AIAA JOURNAL
Vol. 41, No. 2, February 2003

Prediction of Rod–Airfoil Interaction Noise Using the Ffowcs-Williams–Hawkings Analogy

Damiano Casalino,* Marc Jacob,† and Michel Roger‡
Ecole Centrale de Lyon, 69134 Ecully Cedex, France

Sound generated at low Mach number by an airfoil in the wake of a rod is investigated numerically. The Gaussian spanwise loss of coherence of the vortex shedding is shown to have a significant influence on the broadband noise. Spanwise effects are successfully introduced into a time-domain formulation of the Ffowcs-Williams–Hawkings analogy, which is applied to aerodynamic data computed on various contours around the source region. It is shown that a careful choice of these contours is required. The flowfield is obtained from a two-dimensional Reynolds averaged Navier–Stokes calculation. Computed far-field spectra compare very well to measurements obtained in an accompanying experiment.

Nomenclature

C_p	=	pressure coefficient
c	=	airfoil chord
d	=	rod diameter
f	=	frequency
g	=	integration surface, 0
k	=	turbulent kinetic energy
L_g	=	Gaussian correlation length
l	=	span length
M_i	=	Mach number of $g = 0$
M_{oi}	=	observer Mach number vector
M_{ref}	=	reference Mach number
M_∞	=	inflow Mach number
$\hat{n}_i$	=	unit outward normal vector to $g = 0$
p, p_∞	=	pressure and inflow pressure
p_d	=	reference dynamic pressure
p'	=	acoustic pressure
q_i	=	dimensionless relative flow momentum
R	=	dimensionless observation distance
r	=	observation distance
Sr	=	Strouhal number
u_i	=	flow velocity; also (u, v)
$\tilde{u}_i$	=	flow velocity relative to $g = 0$
V_i	=	dimensionless velocity of $g = 0$
V_∞	=	inflow velocity
$\boldsymbol{X}$	=	dimensionless observer position
$\boldsymbol{Y}$	=	dimensionless source position
w	=	Gaussian variance
η	=	spanwise dimensionless co-ordinate
θ	=	observation angle and dimensionless time
λ_i, χ_i	=	loading noise source terms
ρ	=	correlation coefficient
ρ_∞	=	inflow density
ϕ	=	angular rod coordinate
$\tilde{\varphi}$	=	vortex shedding phase

Subscripts

n	=	projection in the normal direction
r	=	projection in the radiation direction

Superscript

$\cdot$	=	dimensionless time derivative

I. Introduction

UNSTEADY aerodynamics of airfoils involve two types of phenomena. One is the flow separation either at the trailing edge or, if the wing is stalled, on the suction side in an otherwise undisturbed flow. The other one is the interaction with oncoming vortical, periodic, or random disturbances. In strongly perturbed flows at reasonable angles of attack, this latter mechanism is dominant in terms of unsteady loading and the resulting sound radiation. Examples of such mechanisms are blade–vortex interactions in helicopter rotors and the wake interactions between blade rows in turbomachinery. A common approach to study these interactions is to decompose the oncoming disturbances into Fourier modes known as gusts and to model the interaction mechanism for each gust (see Refs. 1–3).

Although these gusts are often assumed to be three-dimensional, they are correlated over all of the span, which is infinite. Thus, they do not model any spanwise loss of coherence, which is observed in practical finite span applications. Therefore, one goal of the present study is to model the influence of such effects onto the sound field.

To take into account these three-dimensional effects, an ad hoc spanwise statistical model is introduced into a permeable surface acoustic analogy.[4] In the present paper, the approach is validated on a relevant test configuration: A rod is placed upstream of a symmetric airfoil. The rod sheds a von Kármán street of counter-rotating vortices at a nearly constant Strouhal number $Sr = f_0 d / V_\infty \simeq 0.2$. The resulting flow disturbance is nearly sinusoidal and, thus, can be considered as a gust. In fact, the experiment is operated at quite high rod-based Reynolds numbers ($Re_d = 2.2 \times 10^4$), where the rod wake almost immediately becomes turbulent as the vortices are formed.[5] Thus, the gust that hits the airfoil is more or less periodic with significant spanwise perturbations. The analogy is applied to a two-dimensional unsteady Reynolds averaged Navier–Stokes (RANS) computation and compared to far-field measurements, allowing the three-dimensional model to be validated.

A brief description of the experiment and of the aerodynamic computation is given in Secs. II and III. The aeroacoustic model is discussed in Sec. IV. The computed steady flow and the statistics of its fluctuations are briefly analyzed in Sec. V. In Sec. VI, results of the acoustic analogy are shown: First the influence of the integration surfaces is discussed for a deterministic flow (without the statistical model). Second, the analogy both with and without the spanwise model is tested against experimental data.

Received 24 April 2002; revision received 29 October 2002; accepted for publication 31 October 2002. Copyright © 2002 by the authors. Published by the American Institute of Aeronautics and Astronautics, Inc., with permission. Copies of this paper may be made for personal or internal use, on condition that the copier pay the $10.00 per-copy fee to the Copyright Clearance Center, Inc., 222 Rosewood Drive, Danvers, MA 01923; include the code 0001-1452/03 $10.00 in correspondence with the CCC.

*Aerospace Engineer, Laboratoire de Mécanique des Fluides et d'Acoustique.

†Assistant Professor, Laboratoire de Mécanique des Fluides et d'Acoustique; also Assistant Professor, Institut des Sciences et Technologie de l'Ingénieur de Lyon, Université Claude-Bernard Lyon-I, 43 Bd. Du 11 Nov. 1918, 69100 Villeneuve, France.

‡Professor, Laboratoire de Mécanique des Fluides et d'Acoustique.

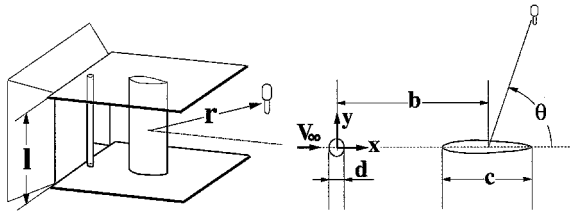

a) Overview b) In-plane view

Fig. 1 Rod–airfoil configuration and experimental setup, where $d = 0.016$ m, $c = 0.1$ m, $b = 0.162$ m, $l = 0.3$ m, $r = 1.38$ m, and $V_\infty = 20$ m/s; airfoil chord parallel to the inflow direction.

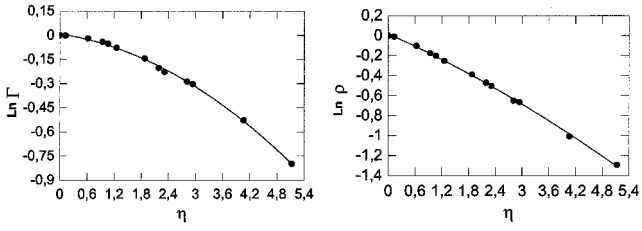

a) Coherence function Γ b) Correlation coefficient ρ

Fig. 2 Spanwise coherence and correlation coefficient on the rod: ●, experimental data and ——, Gaussian interpolation.

II. Experiment

The rod–airfoil experiment is carried out in the small anechoic open jet wind tunnel of the Ecole Centrale de Lyon. The experiment is meant to provide data against which aeroacoustic numerical results can be checked.

The experimental setup is shown in Fig. 1. The reference configuration is a NACA-0012 airfoil downstream of a rod. Both the airfoil and the rod are fixed between two side plates in the potential core of the rectangular jet. The inflow velocity is $V_\infty = 20$ m/s, that is, $M_\infty = 0.06$. The rod diameter is $d = 0.016$ m, and the airfoil chord is $c = 0.1$ m, which provides Reynolds numbers $Re_d = 2.2 \times 10^4$ and $Re_c = 1.37 \times 10^5$, respectively. The distance between the airfoil midpoint and the center of the rod is $b = 0.162$ m. Both the airfoil and the rod extend $l = 0.3$ m in the spanwise direction.

Acoustic measurements are performed at a distance $r = 1.38$ m from the airfoil midpoint, at various observation angles in the midspan plane. A Brüel and Kjäer Type 4191 microphone with a Brüel and Kjäer Type 2669 preamplifier is used for these measurements. Data acquisitions are carried out with a spectral resolution of 2 Hz, from 0 to 6400 Hz, and the number of averages is 300. The Brüel and Kjäer software Pulse is used for the signal acquisition and processing. The rod-alone configuration noise (no airfoil) is also measured to check the airfoil contribution to the rod–airfoil configuration noise. When the uncertainties are taken into account in the geometrical parameters and ambient conditions of temperature and velocity, as well as in the acquisition system, the uncertainty in the measured sound pressure level is 1 dB in the considered frequency range and for observation angles between 45 and 100 deg.

Measurements of wall pressure fluctuations are performed on the rod to investigate the statistical behavior of the vortical flow in the wake of the rod. Six pressure pinholes are drilled on the rod at 90 deg away from the streamwise direction. Hence, two-point statistical measurements are taken with different spacings along the rod span. The coherence at the Strouhal frequency and the correlation coefficient are defined in Appendix A and plotted in Fig. 2. The reference probe is at $\eta = 0$, where η is the spanwise distance from the midspan plane made dimensionless by d. Data are fitted by a Gaussian $\exp(-\eta^2/2L_g^2)$ function, with $L_g = 4.7$ for the coherence function and $L_g = 6.6$ for the correlation coefficient. These lengths differ because all frequencies contribute to the correlation.

III. Aerodynamic Computation

The main goal of the present work is to investigate the feasibility of a low-cost aeroacoustic prediction based on a simplified two-dimensional flow model and an ad hoc model accounting for the three-dimensional statistical behavior of the real flow. Unsteady RANS computations are, thus, performed, that provide only the deterministic component of the unsteady flow. The RANS turbulence model, in fact, acts as a conditioned statistical average that smoothes the random fluctuations, whose effect is only accounted for by an additional turbulent viscosity. The conditioned average requires that a net separation exists between the lowest frequency of the turbulent fluctuations and the highest deterministic frequencies. In other words, the term Reynolds averaged denotes averaging over a time that is longer than that associated with the slowest turbulent motion, but is quite smaller than the vortex shedding period.

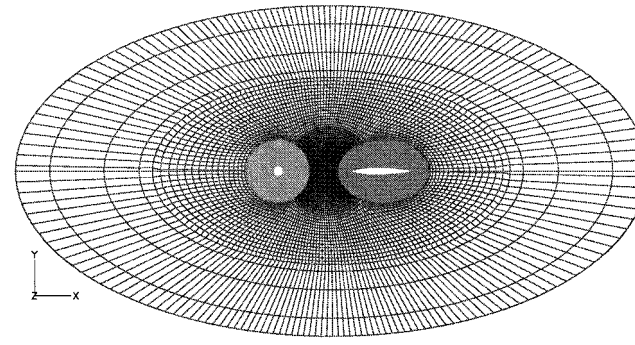

Fig. 3 Overview of computational mesh.

The RANS model used in this study is the two-equation k–ω model proposed by Wilcox,[6] where k is the turbulent kinetic energy and ω is related to the turbulent dissipation. As shown by Cox et al.,[7] this model allows consistent predictions of a circular cylinder flow throughout the shear layer transition regime ($Re_d \lesssim 9 \times 10^4$). Moreover, Boudet et al.[8] found that different RANS models provide quite similar rod–airfoil results.

The compressible finite volume code Proust[9] is used in the current investigation. Both the convective fluxes and the viscous terms are evaluated by using a second-order centered scheme. The solution is advanced in time by using an explicit second-order scheme based on a five-step Runge–Kutta factorization. Nonreflecting boundary conditions and grid stretching in the outer domains are used to limit spurious reflections of acoustic waves. The inflow conditions and the flow parameters are $\rho_\infty = 1.225$ kg/m^3, $V_\infty = 20$ m/s, $p_\infty = 101{,}253.6$ Pa, and $\mu_\infty = 1.78 \times 10^{-5}$ kg/ms. The turbulent kinetic energy has a uniform initial value of 1%, as measured in experiments. The inflow boundary conditions remain the same throughout the computation. An approximated steady potential flow is used as the initial solution. Furthermore, a strong line vortex in the proximity of one rod separation point is added to the initial field to induce a vortex shedding as soon as the computation is started.

The computational mesh is based on 54,640 grid points and is split into five structured domains. An overview of the mesh is plotted in Fig. 3. The grid around the rod is circumferentially clustered in the wake region. The minimum circumferential spacing, at the rod base point $\phi = 0$, is $9.07 \times 10^{-3}\, d$, and the thickness of the mesh wall layer is $7.50 \times 10^{-4}\, d$. The airfoil grid is built around a NACA-0012 airfoil. The thickness of the mesh wall layer varies from $6.40 \times 10^{-5}\, c$, at the leading edge, to $1.42 \times 10^{-3}\, c$, at the thickest airfoil section. A parallel computation is performed with one processor per domain. The computational time step is 6×10^{-8} s, corresponding to about 6.5×10^4 iterations per aerodynamic cycle. There are 1024 aerodynamic fields stored for the acoustic computation, covering 3.15×10^{-2} s.

IV. Acoustic Computation and Spanwise Statistical Model

The rotor noise code Advantia[10] is used for the acoustic prediction. Only surface integrals are computed here because at low Mach numbers the volume sources give a negligible contribution to the acoustic radiation. The consistency of this approximation is checked by comparing acoustic results obtained from different integration surfaces. For the sake of the present work Advantia exploits the retarded time penetrable Ffowcs-Williams–Hawkings (FW–H)

formulation proposed by Brentner and Farassat,[4] extended to a moving observer by Casalino.[10]

When reference length l_{ref}, velocity U_{ref}, time $l_{\text{ref}}/U_{\text{ref}}$, and dynamic pressure p_d are introduced, the thickness and loading noise expressions, for example, p'_Q and p'_L, take the form

$$\frac{2\pi}{p_d}p'_Q(\boldsymbol{X},\theta)=\int_{g=0}\left[\frac{\dot{V}_i\hat{n}_i+\dot{q}_i\hat{n}_i+(V_i+q_i)\dot{\hat{n}}_i}{R(1-M_r)^2}\right]_{\text{ret}}\mathrm{d}S$$
$$+\int_{g=0}\left[\frac{(V_n+q_n)\left\{R\dot{M}_r+\left(M_r-M^2\right)/M_{\text{ref}}\right\}}{R^2(1-M_r)^3}\right]_{\text{ret}}\mathrm{d}S$$
$$-\int_{g=0}\left[M_{or}\frac{\dot{V}_i\hat{n}_i+\dot{q}_i\hat{n}_i+(V_i+q_i)\dot{\hat{n}}_i}{R(1-M_r)^2}\right]_{\text{ret}}\mathrm{d}S$$
$$-\int_{g=0}\left[\frac{M_{or}\dot{M}_r(V_n+q_n)}{R(1-M_r)^3}\right]_{\text{ret}}\mathrm{d}S$$
$$-\int_{g=0}\left[\frac{M_{or}(V_n+q_n)}{R^2(1-M_r)^3M_{\text{ref}}}\left\{2M_r-M^2-M_r^2\right\}\right]_{\text{ret}}\mathrm{d}S$$
$$+\int_{g=0}\left[\frac{M_{oi}M_i(V_n+q_n)}{R^2(1-M_r)^2M_{\text{ref}}}\right]_{\text{ret}}\mathrm{d}S$$
$$-\int_{g=0}\left[\frac{M_{or}(V_n+q_n)}{R^2(1-M_r)M_{\text{ref}}}\right]_{\text{ret}}\mathrm{d}S \tag{1}$$

$$\frac{2\pi}{p_d}p'_L(\boldsymbol{X},\theta)=\int_{g=0}\left[\frac{M_{\text{ref}}\chi_r}{R(1-M_r)^2}\right]_{\text{ret}}\mathrm{d}S$$
$$+\int_{g=0}\left[\frac{\lambda_r-\lambda_M}{R^2(1-M_r)^2}\right]_{\text{ret}}\mathrm{d}S$$
$$+\int_{g=0}\left[\frac{M_{\text{ref}}\lambda_r\left\{R\dot{M}_r+\left[\left(M_r-M^2\right)/M_{\text{ref}}\right]\right\}}{R^2(1-M_r)^3}\right]_{\text{ret}}\mathrm{d}S \tag{2}$$

Dots on quantities denote time derivatives with respect to the dimensionless source time. Large brackets enclose quantities evaluated at the retarded time θ_{ret} obtained from the dimensionless retarded time equation

$$\theta_{\text{ret}}=\theta-[\boldsymbol{X}(\theta)-\boldsymbol{Y}(\theta_{\text{ret}})]M_{\text{ref}} \tag{3}$$

Quantities in Eqs. (1) and (2) are all defined in Appendix B.

There are 1024 aerodynamic fields used for the acoustic computation (about 9 vortex shedding cycles, $t_{\text{fin}}=3.15\times10^{-2}$ s, and $\Delta f=32.5$ Hz). The observation distance from the airfoil midpoint is $r=1.38$ m, and $kr=6.37$ for a typical Strouhal number $Sr=0.2$. Both the observer $\boldsymbol{X}$ and the integration surface $g=0$ move at the constant velocity $c\boldsymbol{M}_o=-V_\infty\hat{\boldsymbol{i}}$, and the flow at infinity is at rest.

Integrations are performed either on the rod and airfoil surfaces, or on penetrable surfaces around the airfoil and the rod–airfoil system. The aerodynamic field on both physical and penetrable surfaces is taken directly from the computational fluid dynamics (CFD) solution. In addition, the aerodynamic data are interpolated on penetrable surfaces that do not coincide with mesh surfaces.

To deal with truncated time series, data are multiplied by the Tukey weighting function $w(t)=0.815[1-\cos(2\pi t/t_{\text{fin}})]$ before performing Fourier analyses. The energy of the original signals is preserved by scaling the windowed data.

The flow past a circular cylinder remains two-dimensional up to Reynolds numbers of about 180. At higher values, three-dimensional fluctuations are superimposed on the dominant vortex shedding, and the wall pressure signals exhibit a random amplitude modulation.

At very low Reynolds numbers, this behavior is presumably related[11] to a cellular structure of the vortex shedding, accompanied by vortex dislocations and oblique vortex shedding. At higher Reynolds numbers cellular shedding has never been observed, despite that pressure and velocity signals exhibit a randomly modulated behavior.[12]

An oblique vortex shedding causes a spanwise variation of the vortex shedding phase. Furthermore, as shown by Casalino,[13] a statistical analogy exists between a random amplitude modulation and a spanwise dispersion of the vortex shedding phase. Hence, an ad hoc statistical model for the vortex shedding phase was proposed by Casalino.[13] The model permits the performance of aeroacoustic predictions through a two-dimensional aerodynamic computation, but accounts to some extent for the three-dimensional character of the flow. It is based on a relationship between the statistical properties of a given spanwise random dispersion of the vortex shedding phase and a given spanwise loss of coherence.

Denoting as $\rho(\eta)$ the correlation coefficient at the vortex shedding frequency and by $w(\eta)$ the variance distribution of the vortex shedding phase $\tilde{\varphi}$ results in

$$w(\eta)=-2\ell_n\{\rho(\eta)\} \tag{4}$$

In particular, a Gaussian dispersion of $\tilde{\varphi}$ with a quadratic variance distribution, that is,

$$w(\eta)=w_{\max}[(2d/l)\eta]^2 \tag{5}$$

provides the Gaussian correlation coefficient

$$\rho=\exp\left(-\eta^2/2L_g^2\right) \tag{6}$$

with

$$w_{\max}=[2(d/l)L_g]^{-2} \tag{7}$$

The correlation length L_g can be experimentally determined and related to the maximum value $w_{\max}$ of the variance at the rod extremities. Details of the spanwise statistical model are given in Appendix A.

Equation (4) provides the variance law that can be used to generate a random phase sequence $\tilde{\varphi}(\eta_i,\tau_j)$ along the rod span. Consistent with the observed features of the vortex shedding process, phase jumps are allowed to occur sporadically every two–three aerodynamic cycles. Furthermore, jump synchronization at two different spanwise sections is avoided by randomizing the time at which the phase jump occurs. The random phase is then converted into a random perturbation of the retarded time by

$$\tilde{\theta}_{\text{ret}}(\eta,\theta)=\theta_{\text{ret}}(\eta)+\frac{\tilde{\varphi}[\eta,\theta_{\text{ret}}(\eta)]}{2\pi\,Sr} \tag{8}$$

where $\theta_{\text{ret}}(\eta)$ denotes the deterministic retarded time defined in Eq. (3).

The aeroacoustic prediction is then performed by forcing into Eqs. (1) and (2) a spanwise random dispersion of the retarded time $\tilde{\theta}_{\text{ret}}(\eta,\theta)$. This is equivalent to introducing a loss of coherence into the spanwise repetition of the two-dimensional aerodynamic field. Interestingly, the same two-dimensional aerodynamic field can be used with different realizations of the random phase distribution. Then averaged acoustic spectra can be computed in a way similar to the experiments.

In the present study, a Gaussian correlation length $L_g=5d$ is used for both the rod and the airfoil, and the acoustic spectra are obtained by averaging over 100 spectra. This value of L_g is close to the value of 4.7 measured for the coherence at the Strouhal frequency. (The coherence function, rather than the correlation coefficient, is representative of the vortex shedding statistics.) The slight overestimate accounts for the spectral broadening around the Strouhal frequency. Because the spanwise correlation decreases far from the rod, using the same value of L_g for both the airfoil and the rod provides an overestimate of the airfoil noise contribution. In the present configuration, such an overestimate is within the experimental uncertainty. However, for higher values of the ratio b/d, the local correlation length in the rod wake at the airfoil leading edge should be used for the acoustic computation.

V. Aerodynamic Results

A snapshot of the enstrophy field in Fig. 4 shows a vortex street downstream of the rod, undergoing a nearly direct interaction with the airfoil leading edge. Such a vortical flow induces the force plotted in Fig. 5 on the rod–airfoil system. Both the rod and the airfoil lift depend on the vortex sign, whereas the drag does not. Hence, the lift and the drag main frequencies are $f_0 \simeq 300$ Hz and $2f_0$, respectively. The airfoil lift is about six times higher than the rod lift.

Counter-rotating vortices are shed from the rod at a Strouhal number $Sr = 0.24$. The overestimate of the vortex shedding frequency from a two-dimensional rod is a common CFD result[14] that can be explained to some extent. As argued by Roshko,[15] the length of the mean recirculating region behind the rod results from an equilibrium between the base suction coefficient and the in-plane Reynolds stresses in the separated flow region. Therefore, higher Reynolds stresses correspond to shorter mean recirculating regions. In a three-dimensional flow, a part of the energy is extracted from the mean flow to sustain spanwise velocity fluctuations. As a consequence, the mean recirculating region extends farther from the cylinder, and the Strouhal frequency is smaller than in a computed two-dimensional flow.

Let $\langle\ \rangle$ denote the local average of a quantity over a vortex shedding period; the following quantities are plotted in Figs. 6–8.

Mean pressure coefficient:

$$\langle C_p \rangle = \frac{\langle p - p_\infty \rangle}{\frac{1}{2}\rho_\infty V_\infty^2} \tag{9}$$

Root-mean-square pressure coefficient:

$$C_{p_{\text{rms}}} = \sqrt{\left\langle (C_p - \langle C_p \rangle)^2 \right\rangle} \tag{10}$$

Dimensionless mean velocity:

$$\langle V \rangle = \sqrt{\langle u \rangle^2 + \langle v \rangle^2} \Big/ V_\infty \tag{11}$$

Dimensionless root-mean-square velocity:

$$V_{\text{rms}} = \sqrt{\left\langle (u n_x / V_\infty + v n_y / V_\infty - \langle V \rangle)^2 \right\rangle + \tfrac{2}{3}\langle k \rangle} \tag{12}$$

where $n_x = \langle u \rangle / \langle V \rangle$ and $n_y = \langle v \rangle / \langle V \rangle$ are the components of the mean flow direction and $\langle k \rangle$ denotes the mean turbulent kinetic energy. [Equation (12) is based on the hypothesis of local isotropy of the turbulent velocity field, that is, $k = \frac{3}{2}\overline{u'u'}$, where u' is the Reynolds fluctuating component of the velocity field in the x direction. Clearly, in the framework of unsteady RANS modeling, a fluctuating k makes sense only if the averaging time is longer than that associated with the slowest turbulent motions, but is much smaller than the timescale of the unsteady flow. (The vortex shedding period in the present study.)]

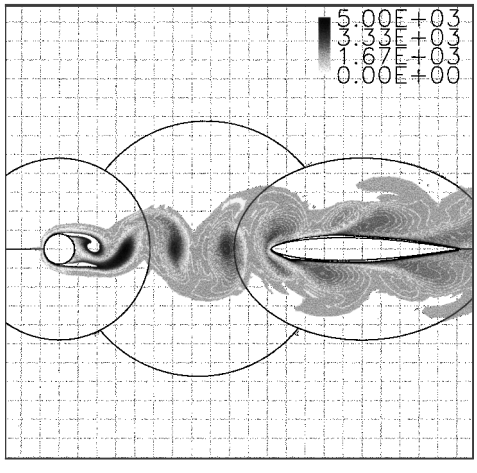

Fig. 4 Enstrophy field around the rod–airfoil system; grid spacings every 1×10^{-2} m.

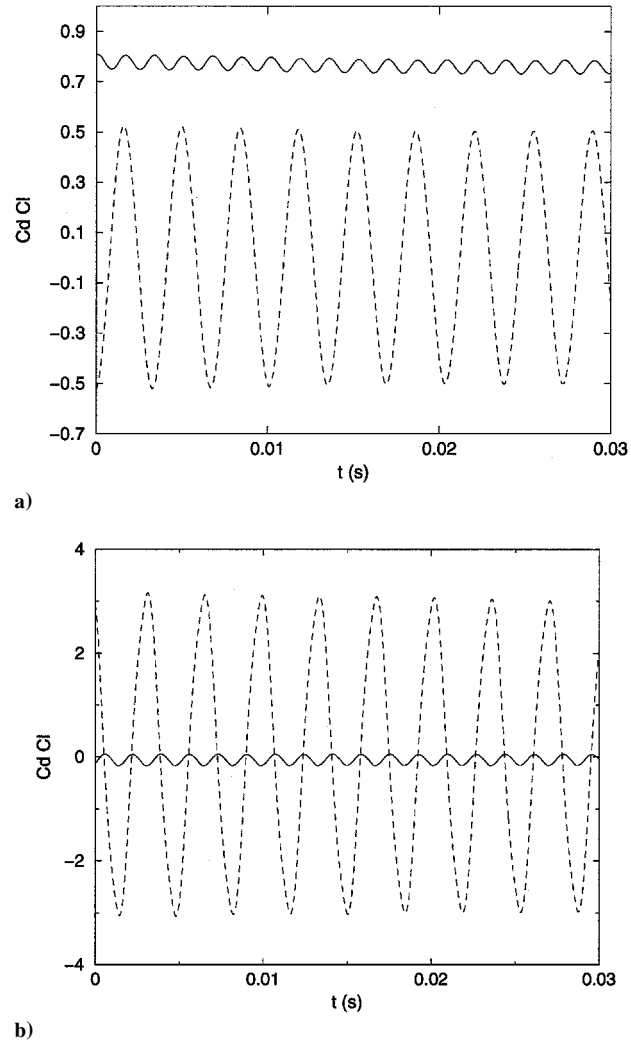

Fig. 5 Reference length d, force on a) rod and b) airfoil: ——, C_d and - - - -, C_l.

In Fig. 6a the mean velocity past the rod shows the recirculating region behind the rod. The downstream point of minimum $\langle V \rangle$ at $x/d = 1.27$, $y = 0$ coincides with the point of maximum V_{rms}, as shown by Fig. 6b. Conventionally, such a point defines the vortex formation length. Measurements made by Szepessy and Bearman[12] over a wide range of Reynolds numbers and rod aspect ratios show a vortex formation length of about 1.5. Therefore, consistently with Roshko's[15] model, a two-dimensional computation provides a smaller mean recirculating region behind the rod.

The mean and fluctuating velocity fields past the airfoil are plotted in Fig. 7. Higher fluctuations occur in a very narrow region close to the leading edge where a strong vortex stretching is accompanied by high-velocity gradients and where the stagnation point oscillates around the leading edge.

Figure 8a shows the pressure field on the rod surface. The $C_{p_{\text{rms}}}$ is maximum at $\phi = 95.5$ deg, which marks the mean location of the separation point. The pressure field on the airfoil surface is plotted in Fig. 8b. $C_{p_{\text{rms}}}$ peaks near the leading edge and decreases rapidly downstream. The fluctuating pressure level at the leading edge is about 159 times higher than that at the trailing edge. Furthermore, the maximum $C_{p_{\text{rms}}}$ on the airfoil is 4.5 times higher than the maximum on the rod. Therefore, the stronger aeroacoustic sources in the rod–airfoil configuration are likely to be found near the airfoil leading edge.

The convergence question has been addressed in two steps to separate the influence of the mesh on the vortex shedding from that on the vortex convection downstream of the rod. First,[13] a circular cylinder flow at the same Reynolds number was predicted by using a quite finer mesh (197×193 O grid, stretched up to 20 rod diameters). The same values of Strouhal number and vortex formation

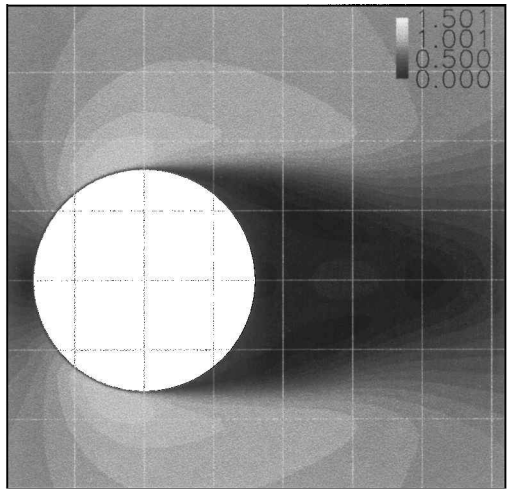

a) $\langle V \rangle$

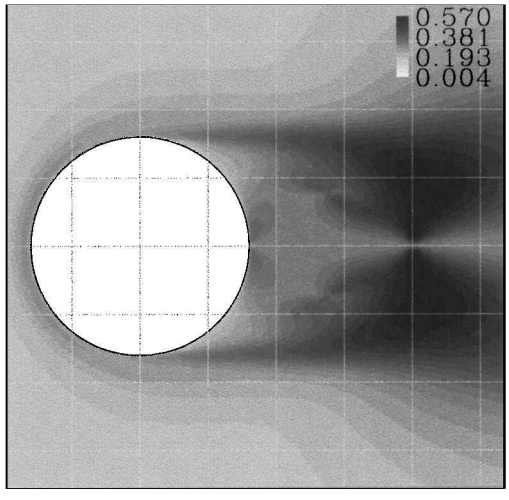

b) V_{rms}

Fig. 6 Mean and fluctuating flow past the rod; grid spacings every 5×10^{-3} m.

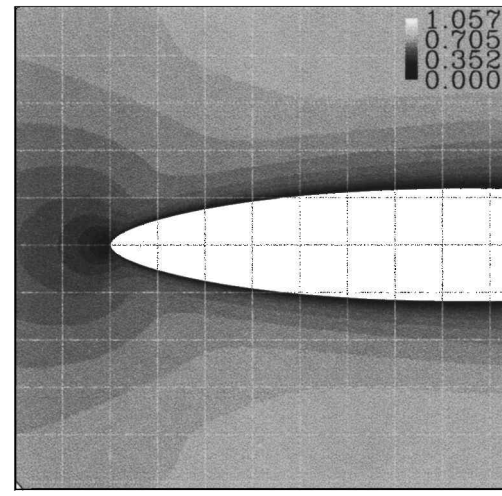

a) $\langle V \rangle$

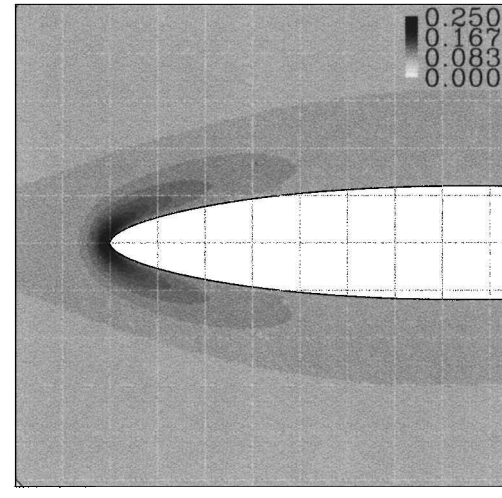

b) V_{rms}

Fig. 7 Mean and fluctuating flow past the airfoil; grid spacings every 5×10^{-3} m.

length were obtained. Second,[8] the rod–airfoil problem at a higher Reynolds number ($Re_d = 4.9 \times 10^4$) but still in the shear layer transition regime was attacked with a finer mesh (about 65,000 grid points). Similar unsteady mechanisms were observed, specifically the same influence of the airfoil on the upstream vortex trajectories was predicted.

VI. Acoustic Results

The integration surfaces used in the present investigation are plotted in Fig. 9. They are denoted as R, rod physical surface (200 points); A1, . . . , A4, surfaces around the airfoil coinciding with lines of the CFD mesh (200 points), where A1 is the airfoil surface and the others are at increasing distance; RAint1, . . . , RAint4, surfaces around the rod–airfoil, from the nearest to the farthest, not fitting the CFD mesh, where the aerodynamic data are interpolated from the CFD solution (520 points); and RAcfd, surface around the rod–airfoil coinciding with lines of the CFD mesh (595 points).

A. Influence of Integration Surface

In this subsection, acoustic computations are performed on the base of a two-dimensional flow (no spanwise effect).

Figures 10–13 show the acoustic spectrum at $\theta = 90$ deg obtained from different integration surfaces.

First, the rod R and the airfoil A1 contributions are compared in Fig. 10 to the noise obtained by integration on RAint1, which surrounds the rod–airfoil system. The aerodynamic data on RAint1 are obtained from a spatial linear interpolation of the CFD solution. This causes an unphysical behavior at 1000 Hz $\lesssim f$, which is attributed to that the instantaneous interpolation does not account for the convective delay between the solution at two points. As shown in Fig. 11, integrations on RAint1, . . . , RAint4 provide unphysical but consistent results.

Then, results obtained by integrating on A1, . . . , A4 around the airfoil are compared in Fig. 12. Only small differences appear at even harmonics, showing again the consistency of the penetrable FW–H formulation.

Finally, in Fig. 13 the rod R and the airfoil A1 contributions are compared to that obtained from the surface RAcfd, which is taken from the CFD mesh and surrounds the rod–airfoil system. Now, the rod–airfoil spectrum exhibits a physically reliable behavior.

Figure 13 shows that at $\theta = 90$ deg the airfoil is $86.9 - 71.1 = 15.8$ dB louder than the rod. Because at the present Mach number the acoustic radiation is essentially dipolar, such a difference should correspond to an airfoil–rod lift amplitude ratio of 6.16. This value is in good agreement with that found in Fig. 5.

In Fig. 14, the rod R and the airfoil A1 acoustic signals are checked against that obtained from RAcfd. Surprisingly, the rod–airfoil system is quieter than the airfoil alone. This is because the rod and the airfoil signals are in a partial phase opposition and because the computed shedding and the rod wake are deterministic.

To check further the consistency of the penetrable FW–H prediction, Fig. 15 shows the relative difference between the RAcfd noise and the sum of the rod R and the airfoil A1 contributions. The spectrum of $\Delta p'/\max(p')$ exhibits an enveloped broadband behavior with harmonics peaks, the even ones being slightly higher. Such a difference may be due to numerical as well as physical effects,

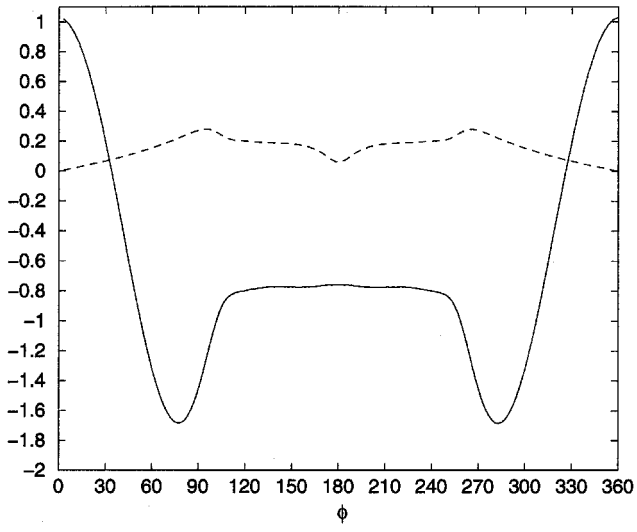

a) Rod

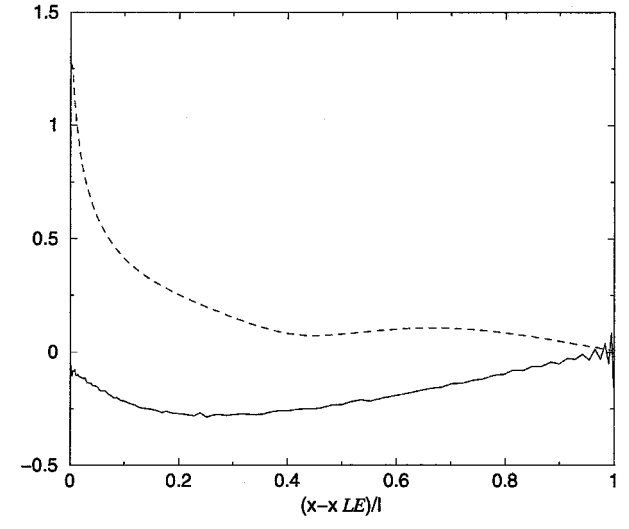

b) Airfoil

Fig. 8 Pressure field where $\phi = 180$ deg denotes the forward stagnation point on the rod and x_{LE} is the airfoil leading edge: ——, $\langle C_p \rangle$ and - - - -, $C_{p_{rms}}$.

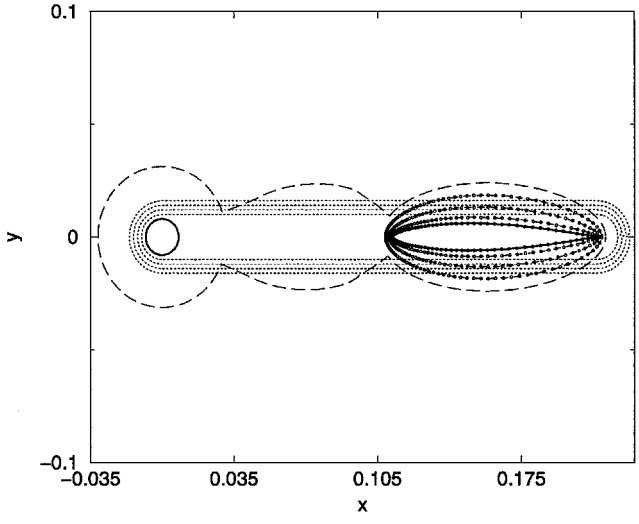

Fig. 9 Integration surfaces: ——, R; ●, A1, . . . , A4; - - - -, RAint1, . . . , RAint4; and − − −, RAcfd.

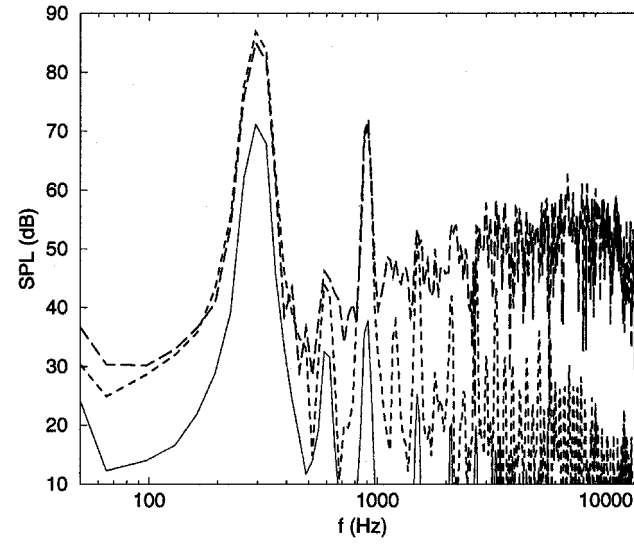

Fig. 10 Acoustic spectrum at $\theta = 90$ deg; two-dimensional aerodynamic field, integrations on ——, R; - - - -, A1; and − − −, RAint1.

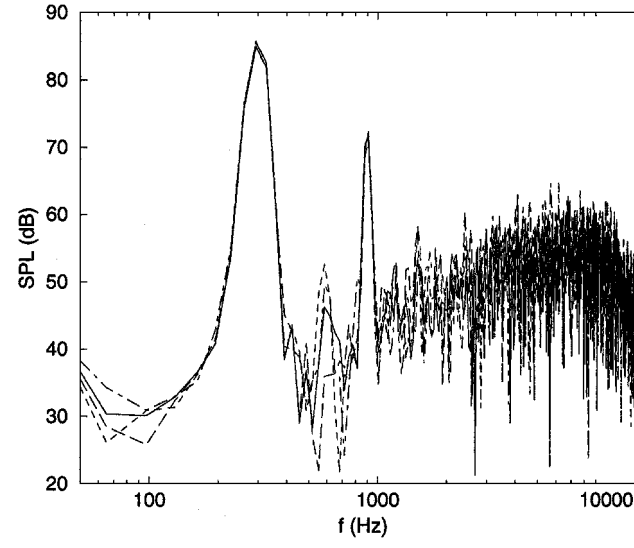

Fig. 11 Acoustic spectrum at $\theta = 90$ deg; two-dimensional aerodynamic field, integrations on RAint1, . . . ,RAint4.

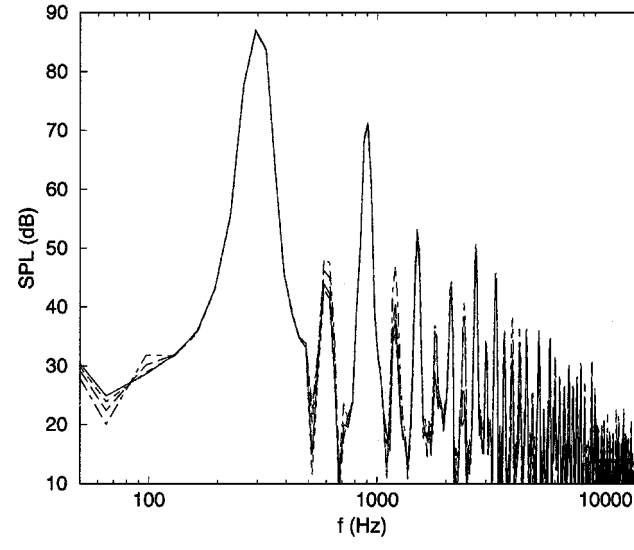

Fig. 12 Acoustic spectrum at $\theta = 90$ deg; two-dimensional aerodynamic field, integrations on A1, . . . , A4.

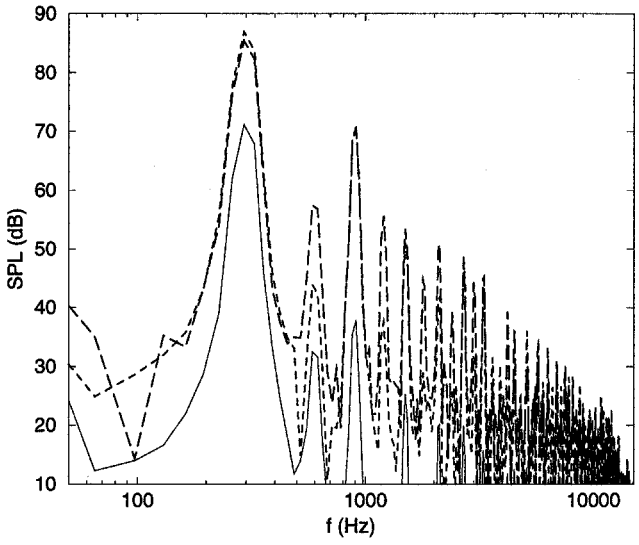

Fig. 13 Acoustic spectrum at $\theta = 90$ deg; two dimensional aerodynamic field, integrations on ——, R; - - - -, A1; and – – –, RAcfd.

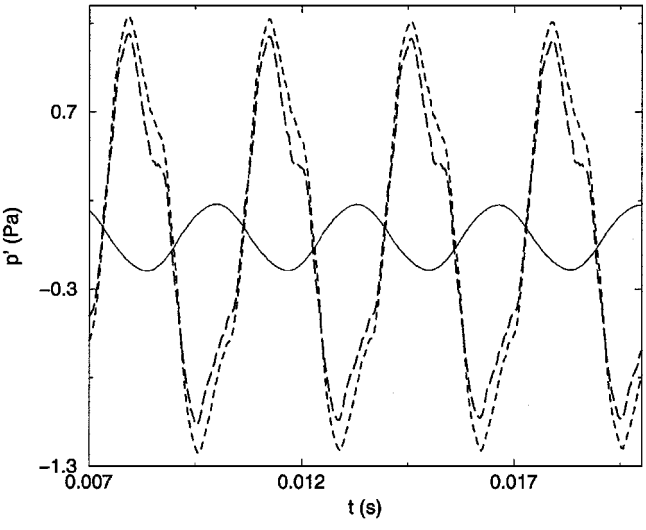

Fig. 14 Acoustic signals at $\theta = 90$ deg; two dimensional aerodynamic field, ——, rod; - - - -, airfoil; and – – –, rod–airfoil.

namely, nonlinear contributions from the flowfield inside RAcfd. The even harmonics effect also has been observed in Fig. 12 by integrating on surfaces surrounding the airfoil alone. This plays in favor of the possible physical reliability of Fig. 15.

B. Comparison with Acoustic Measurements

In this subsection acoustic computations are performed by forcing statistical three-dimensional effects into the aerodynamic field. In Figs. 16 and 17, acoustic results are checked against experimental data. Both the rod-alone and the rod–airfoil noise are plotted. The computed rod–airfoil noise is indeed the airfoil contribution obtained from A1. This approximation can be justified by invoking the small difference found between the airfoil-alone and the rod–airfoil noise. Such a difference is even smaller in the reality because the deterministic phase opposition is smeared by some random effects.

The numerical predictions are performed by considering a two-dimensional aerodynamic field and an aerodynamic field with a Gaussian correlation along the rod and the airfoil spans (three dimensional). The measured power spectral densities have been integrated on intervals of $\Delta f = 32.5$ Hz to provide sound levels against which the numerical ones can be checked. Furthermore, the overestimate of the Strouhal frequency is taken into account by scaling

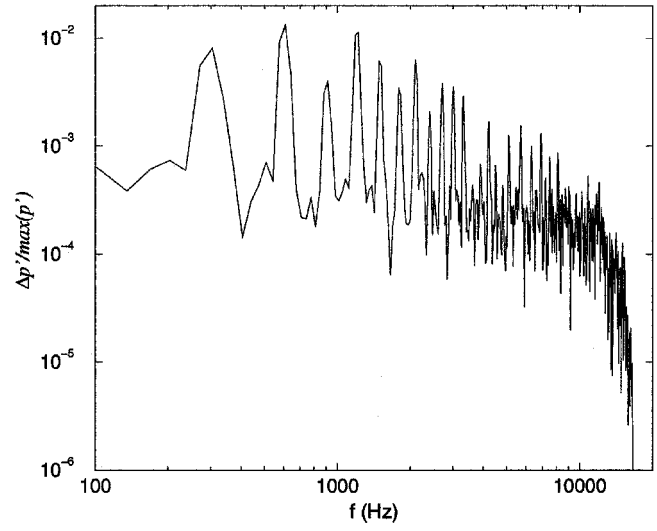

Fig. 15 Spectrum of the relative difference between the rod–airfoil noise RAcfd and the sum of the rod R and the airfoil A1 contributions at $\theta = 90$ deg; two-dimensional aerodynamic field.

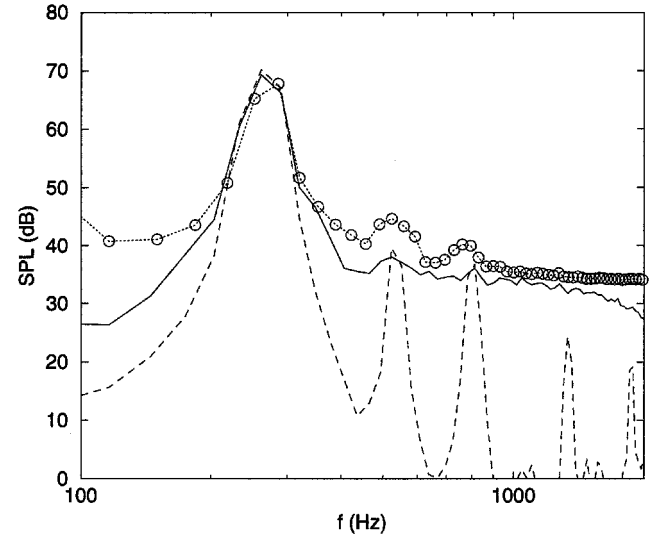

Fig. 16 Rod noise spectrum at $\theta = 90$ deg; comparison between: ○, experimental data; - - - -, two-dimensional prediction; and ——, three-dimensional prediction.

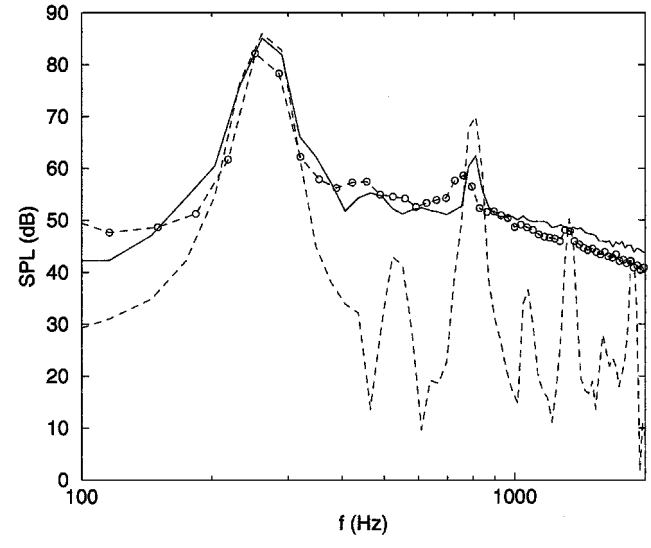

Fig. 17 Rod–airfoil noise spectrum at $\theta = 90$ deg; comparison between, ○, experimental data; - - - -, two-dimensional prediction; and ——, three-dimensional prediction.

the numerical results from (f, decibel) to (f', decibel′), that is,

$$f' = \frac{Sr_{\text{exp}}}{Sr_{\text{num}}} f, \qquad \text{decibel}' = \text{decibel} + 20\log\left(\frac{Sr_{\text{exp}}}{Sr_{\text{num}}}\right) \quad (13)$$

where the level correction accounts for the sound level being proportional to the vortex shedding frequency.

In Fig. 16, the rod noise spectrum at $\theta = 90$ deg is plotted. The Strouhal peak is well predicted by both the two- and three-dimensional computations. Conversely, the second and third harmonic peaks are not well predicted. Comparing two- and three-dimensional results shows that the statistical model allows a quite accurate prediction of the broadband spectral behavior. This is because the spanwise random distribution of the vortex shedding phase results in a random amplitude modulation of the acoustic signal. The second and third harmonic levels in the measurements are likely to be contaminated by installation effects. Indeed, as shown in Fig. 1a, the rod is slightly downstream of the duct termination. Hence, some diffraction effects may be responsible for a slight different acoustic behavior with respect to that of an isolated rod.

In Fig. 17, the rod–airfoil noise spectrum at $\theta = 90$ deg is plotted. Computations provide an overestimate of about 3 dB of the Strouhal peak. This is not surprising for the airfoil-alone prediction. In fact, as discussed earlier, the rod–airfoil system is about 2 dB quieter than the airfoil alone. The three-dimensional results show improvements in the prediction of the third harmonic peak. Moreover, the broadband spectral behaviour is quite well featured by the three-dimensional computation.

C. Uncertainty in the Acoustic Prediction

The uncertainty in the present acoustic analogy computation depends essentially on four factors: 1) the influence of the volume sources that are not accounted for, 2) the influence of the jet refraction effects that are not accounted for, 3) the accuracy of the integral computation, and 4) the uncertainty in the near-field aerodynamic quantities.

The first item has been addressed by considering different integration surfaces and by comparing the predicted acoustic spectra. The volume sources contribution can be neglected paying for an uncertainty of about 0.1 dB.

The jet refraction effects have been neglected by supposing that both the observer and the source move at the same velocity in a medium at rest. As shown by Amiet,[16] the error introduced by this approximation is of order M_∞^2; therefore, it is not significant in the present study.

The accuracy of the integral computation depends on the number of discrete elements and the quality of the interpolation used when the points of the integration surface do not coincide with those of the CFD mesh. Therefore, the best strategy is to use an integration surface filling the CFD mesh. This ensures a high-resolution level and a compatibility condition between the aerodynamic quantities involved in the integral formulation and the discretized flow governing equations. (For an explicit scheme, for example, the Courant–Friedrichs–Lewy condition can be interpreted as a minimum condition for the maximum number of grid points per shortest acoustic wavelength.)

The sensibility of the acoustic results to some aerodynamic quantities can be addressed by considering a simplified aeroacoustic model describing a compact harmonic dipole perpendicular to the flow, undergoing a random phase variation $\tilde{\varphi}$ in the spanwise direction. The acoustic intensity in the geometrical and acoustic far field is proportional to $C_{l\max}^2\,\alpha(L_g)$, where $C_{l\max}$ is the amplitude of the lift fluctuations and

$$\alpha(L_g) = \int_{-d/2l}^{+d/2l}\int_{-d/2l}^{+d/2l} \exp\{-i[\tilde{\varphi}(\eta_1) - \tilde{\varphi}(\eta_2)]\}\,\mathrm{d}\eta_1\,\mathrm{d}\eta_2 \quad (14)$$

accounts for the spanwise variation of the vortex shedding phase. In the present study, the value of $C_{l\max}$ is an aerodynamic result, whereas the value of L_g is determined experimentally and used to generate a Gaussian distribution of $\tilde{\varphi}$ along the body span. Therefore, an assumed uncertainty of 1 dB of the sound pressure level (the experimental uncertainty) corresponds to an uncertainty in $C_{l\max}$ of 12%. The effect of the correlation length can be evaluated by computing the quantity $\Delta\text{dB} = 10\log[\alpha(L_g)/\alpha\{L_{g\,\text{ref}}\}]$. This is plotted against $\delta = L_g/L_{g\,\text{ref}}$ in Fig. 18 for the reference value $L_{g\,\text{ref}} = 5$. An uncertainty of 1 dB around the reference value (±0.5 dB) of the sound pressure level corresponds to an uncertainty in L_g of 20%.

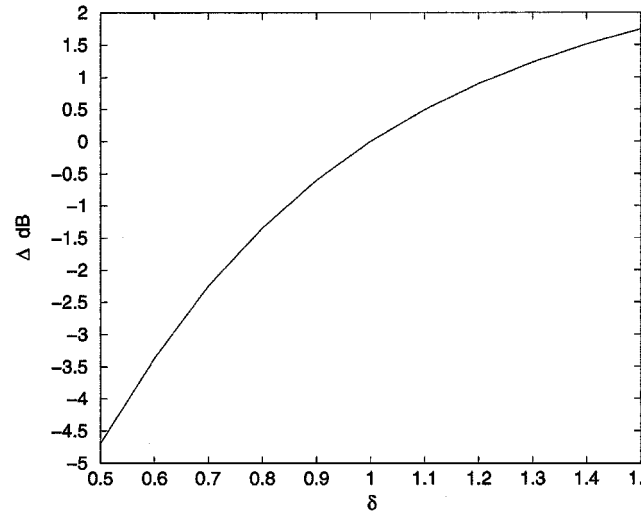

Fig. 18 Influence of the correlation length on the sound pressure level.

Because the actual errors on $C_{l\max}$ and L_g are much less than the aforementioned values 12 and 20%, the uncertainty in the acoustic computation is lower than 1 dB.

VII. Conclusions

This study shows how a statistical model can be used in a time-domain acoustic analogy to account for three-dimensional spanwise effects that are not featured by a two-dimensional flow computation. Sound predictions are significantly improved, and the broadband part of the sound field is quite well predicted. The model requires only an a priori knowledge of the spanwise correlation length and shape.

The spanwise statistical model is here applied to a rod–airfoil configuration. It is shown that the airfoil contribution is dominant and gives a good estimate of the overall noise. A particular point is that a fully correlated (two-dimensional) sound computation predicts partial cancellations between the rod and the airfoil contributions that are not likely to exist in the real three-dimensional flow.

Interesting results are found or confirmed about the choice of a suitable integration surface:

1) It should be constituted by grid points of the CFD domain.

2) In low-Mach-number applications, volume sources are negligible with respect to surface sources, and the physical surfaces are the best-suited integration surfaces.

The statistical analogy is an interesting tool for complex flow configurations where only unsteady but deterministic RANS computations can be carried out.

Appendix A: Coherence and Correlation

The coherence function Γ_{xy} between two signals $x(t)$ and $y(t)$ is defined as

$$\Gamma_{xy}(f) = \frac{|S_{xy}(f)|}{\sqrt{S_{xx}(f)S_{yy}(f)}} \quad (A1)$$

where $S_{xy}(f)$ is the cross-power spectral density $S_{xy}(f) = \text{TF}\{C_{xy}(\tau)\}$, with

$$C_{xy}(\tau) = \lim_{T\to\infty}\frac{1}{T}\int_0^T x(t)\,y(t-\tau)\,\mathrm{d}t \quad (A2)$$

and TF denotes Fourier transform. For an ergodic process $C_{xy}(\tau)$ can be interpreted as the correlation function between $x(t)$ and $y(t)$.

The correlation coefficient ρ is defined as

$$\rho = \frac{C_{xy}(0)}{\sqrt{C_{xx}(0)\,C_{yy}(0)}} = \frac{\int_{-\infty}^{\infty} S_{xy}(f)\,\mathrm{d}f}{\sqrt{\int_{-\infty}^{\infty} S_{xx}(f)\,\mathrm{d}f}\sqrt{\int_{-\infty}^{\infty} S_{yy}(f)\,\mathrm{d}f}} \tag{A3}$$

In the case of two tuned monochromatic signals, it results that $\rho = \Gamma_{xy}(f_0)$.

The fluctuating pressure on the rod surface at 90 deg away from the streamwise direction is representative of the fluctuating lift behavior. Thus, considering two points at different spanwise locations, the pressure signals can be written as $p_1(t) = P\cos(2\pi f_0 t + \tilde{\varphi}_1)$ and $p_2(t) = P\cos(2\pi f_0 t + \tilde{\varphi}_2)$, where $\tilde{\varphi}$ accounts for a random spanwise phase variation. The corresponding cross-correlation function is given by

$$\begin{aligned} C_{12}(\Theta) &= \mathcal{E}[p_1(t)\,p_2(t+\Theta)] \\ &= (P^2/2)\mathcal{E}[\cos\tilde{\varphi}_1\cos\tilde{\varphi}_2]\cos(2\pi f_0\Theta) \\ &\quad - (P^2/2)\mathcal{E}[\cos\tilde{\varphi}_1\sin\tilde{\varphi}_2]\sin(2\pi f_0\Theta) \\ &\quad + (P^2/2)\mathcal{E}[\sin\tilde{\varphi}_1\cos\tilde{\varphi}_2]\sin(2\pi f_0\Theta) \\ &\quad + (P^2/2)\mathcal{E}[\sin\tilde{\varphi}_1\sin\tilde{\varphi}_2]\cos(2\pi f_0\Theta) \end{aligned} \tag{A4}$$

where $\mathcal{E}[\,]$ denotes the expected value.

Because the flow can be supposed to be statistically homogeneous along the rod span, the phase shift $\tilde{\varphi} = \tilde{\varphi}_2 - \tilde{\varphi}_1$ depends only on the separation distance $\eta = \eta_2 - \eta_1$. Therefore, we can take the reference point at the rod half-span, $\eta_1 = 0$, and consider only the random variable $\tilde{\varphi}(\eta)$. Substitution in Eq. (A4) yields

$$\begin{aligned} C_{12}(\Theta) &= (P^2/2)\mathcal{E}[\cos\tilde{\varphi}]\cos(2\pi f_0\,\Theta) \\ &\quad - (P^2/2)\mathcal{E}[\sin\tilde{\varphi}]\sin(2\pi f_0\Theta) \end{aligned} \tag{A5}$$

whose corresponding correlation coefficient is

$$\rho(\eta) \equiv C_{12}(0) = \mathcal{E}[\cos\tilde{\varphi}] \tag{A6}$$

Moreover, the coherence function is given by

$$\begin{aligned} \Gamma(\eta, f) &= \frac{|S_{12}(\eta, f)|}{\sqrt{S_{11}}\sqrt{S_{22}}} \\ &= \mathcal{E}[\cos\tilde{\varphi}]\delta(f - f_0) - \mathcal{E}[\sin\tilde{\varphi}]\delta(f - f_0) \end{aligned} \tag{A7}$$

Note that for a symmetric probability density of $\tilde{\varphi}$ it results that $\mathcal{E}[\sin\tilde{\varphi}] = 0$ and that the coherence function can be interpreted as the correlation coefficient, that is,

$$\Gamma(\eta, f) = \rho(\eta)\delta(f - f_0) \tag{A8}$$

The random distribution of the spanwise phase shift $\tilde{\varphi}$ is reasonably expected to have a Gaussian probability density $\mathcal{P}$, that is,

$$\mathcal{P}(\tilde{\varphi}, \eta) = \frac{\exp[-\tilde{\varphi}^2/2\,w(\eta)]}{\sqrt{2\pi\,w(\eta)}} \tag{A9}$$

with variance w vanishing toward the rod half-span and increasing symmetrically toward the rod extremities, $\eta = \pm l/2d$. Now, to determine the correlation coefficient (A6), consider the Taylor series of $\cos\tilde{\varphi}$ and write

$$\mathcal{E}[\cos\tilde{\varphi}] = \mathcal{E}\left[\sum_{n=0}^{\infty}\frac{(-1)^n}{(2n)!}\tilde{\varphi}^{2n}\right] = \sum_{n=0}^{\infty}\frac{(-1)^n}{(2n)!}\mathcal{E}[\tilde{\varphi}^{2n}] \tag{A10}$$

Because $\tilde{\varphi}$ has a Gaussian density probability, it results that

$$\mathcal{E}[\tilde{\varphi}^0] = 1$$

and for $n \geq 1$

$$\mathcal{E}[\tilde{\varphi}^{2n-1}] = 0$$

$$\mathcal{E}[\tilde{\varphi}^{2n}] = (2n-1)(2n-3)\cdots 3\cdot 1\cdot w^n$$

Thus, with substitution into Eq. (24) and performance of some algebra, that is,

$$\begin{aligned} \mathcal{E}[\cos\tilde{\varphi}] &= \sum_{n=0}^{\infty}\frac{(-1)^n}{(2n)!}(2n-1)\cdots 3\cdot 1\cdot w^n \\ &= \sum_{n=0}^{\infty}\frac{(-w)^n}{2n(2n-2)(2n-4)\cdots 4\cdot 2} \\ &= \sum_{n=0}^{\infty}\frac{(-w/2)^n}{n(n-1)(n-2)\cdots 3\cdot 1} \\ &= \sum_{n=0}^{\infty}\frac{1}{n!}\left(-\frac{w}{2}\right)^n \equiv \exp\left(-\frac{w}{2}\right) \end{aligned} \tag{A11}$$

the two-point correlation coefficient takes the form

$$\rho(\eta) = \exp(-w/2) \tag{A12}$$

Appendix B: Symbols in the FW–H Analogy

The aerodynamic field is introduced into Eqs. (1) and (2) in terms of conservative quantities: the flow density ρ; the linear momentum $\rho\tilde{u}_i$, where $\tilde{u}_i$ is the relative velocity of the flow with respect to the integration surface $g = 0$; the specific total internal energy ρE; and the specific turbulent kinetic energy ρk. All of the involved quantities are defined as follows:

$$p_d = \frac{1}{2}\rho_0\,U_{\mathrm{ref}}^2, \qquad \theta = \frac{t\,U_{\mathrm{ref}}}{l_{\mathrm{ref}}}, \qquad M_{\mathrm{ref}} = \frac{U_{\mathrm{ref}}}{c}$$

$$V_i = \frac{v_i}{U_{\mathrm{ref}}}, \qquad V_n = V_i\hat{n}_i, \qquad \tilde{u}_i = u_i - v_i$$

$$\boldsymbol{X} = \frac{\boldsymbol{x}}{l_{\mathrm{ref}}}, \qquad \boldsymbol{Y} = \frac{\boldsymbol{Y}}{l_{\mathrm{ref}}}$$

$$\hat{r}_i = \frac{X_i - Y_i}{|\boldsymbol{X} - \boldsymbol{Y}|}, \qquad R = |\boldsymbol{X} - \boldsymbol{Y}|$$

$$M_i = \frac{v_i}{c}, \qquad M_r = M_i\,\hat{r}_i, \qquad \dot{M}_r = \dot{M}_i\,\hat{r}_i, \qquad M_{or} = M_{oi}\,\hat{r}_i$$

$$\sigma = \frac{\rho}{\rho_0}, \qquad q_i = \frac{(\rho\tilde{u}_i)}{(\rho_0 U_{\mathrm{ref}})}, \qquad e = \frac{(\rho\,E)}{\left(\rho_0 U_{\mathrm{ref}}^2\right)}, \qquad k = \frac{(\rho K)}{\left(\rho_0 U_{\mathrm{ref}}^2\right)}$$

$$C_p = 2\left\{(\gamma - 1)\left[e - \frac{q_i\,q_i}{2\,\sigma} - k\right] - \frac{p_0}{2\,p_d}\right\}$$

$$\dot{C}_p = 2(\gamma - 1)\left[\dot{e} - \frac{q_i\,\dot{q}_i}{\sigma} + \dot{\sigma}\frac{q_i\,q_i}{2\,\sigma^2} - \dot{k}\right]$$

$$\lambda_i = \frac{C_p}{2}\hat{\boldsymbol{n}}_i + V_i\,q_n + \frac{q_i\,q_n}{\sigma}$$

$$\chi_i = \frac{\dot{C}_p}{2}\hat{\boldsymbol{n}}_i + \frac{C_p}{2}\dot{\hat{n}}_i + \dot{V}_i q_n + V_i(\dot{q}_i\hat{\boldsymbol{n}}_i) + V_i(q_i\dot{\hat{\boldsymbol{n}}}_i) + \frac{\dot{q}_i q_n}{\sigma} + \frac{q_i(\dot{q}_i\hat{n}_i)}{\sigma} + \frac{q_i(q_i\dot{\hat{n}}_i)}{\sigma} - \frac{q_i q_n}{\sigma^2}\dot{\sigma}$$

$$q_n = q_i\hat{n}_i, \qquad \lambda_M = \lambda_i\,M_i, \qquad \lambda_r = \lambda_i\,\hat{r}_i, \qquad \chi_r = \chi_i\,\hat{r}_i$$

In these expressions p_0 and ρ_0 are the quiescent fluid pressure and density, respectively, $\boldsymbol{M}_o$ denotes the observer Mach number, $\hat{\boldsymbol{n}}_i$ is the unit vector pointing out of the integration surface and overdots

denote derivatives with respect to the dimensionless time θ. The loading-noise term χ_i is the dimensionless time derivative of λ_i.

Other details concerning the rotor noise code Advantia and the implemented FW–H formulation may be found in Casalino's works.[10,13]

Acknowledgment

This work was partially supported by the European Community as part of the project TurboNoise–CFD.

References

[1]Possio, C., "L'Azione Aerodinamica sul Profilo Oscillante in un Fluido Compressibile a Velocità Iposonora," *L'Aerotecnica*, Vol. 18, No. 4, 1938, pp. 441–458.

[2]Sears, W. R., "Some Aspects of Non-Stationary Airfoil Theory and Its Practical Application," *Journal of the Aeronautical Sciences*, Vol. 8, No. 3, 1941, pp. 104–108.

[3]Graham, J. M. R., "Similarity Rules for Thin Airfoils in Non-Stationary Subsonic Flows," *Journal of Fluid Mechanics*, Vol. 43, No. 4, 1970, pp. 753–766.

[4]Brentner, K. S., and Farassat, F., "Analytical Comparison of the Acoustic Analogy and Kirchhoff Formulation for Moving Surfaces," *AIAA Journal*, Vol. 36, No. 8, 1998, pp. 1379–1386.

[5]Williamson, C. H. K., "Vortex Dynamics in the Cylinder Wake," *Annual Review of Fluid Mechanics*, Vol. 28, 1996, pp. 477–539.

[6]Wilcox, D. C., "Comparison of Two Equations Turbulence Models for Boundary Layers with Pressure Gradient," *AIAA Journal*, Vol. 31, No. 8, 1993, pp. 1414–1421.

[7]Cox, J. S., Rumsey, C. L., and Brentner, K. S., "Computation of Sound Generated by Viscous Flow over a Circular Cylinder," NASA TM 110339, 1997.

[8]Boudet, J., Casalino, D., Jacob, M. C., and Ferrand, P., "Unsteady RANS Computations of the Flow past an Airfoil in the Wake of a Rod," *Proceedings of the ASME Fluids Engineering Division Summer Meeting*, FEDSM02, American Society of Mechanical Engineers, Fairfield, NJ, 2002.

[9]Ferrand, P., Aubert, S., Smati, L., Bron, O., and Atassi, H. M., "Nonlinear Interaction of Upstream Propagating Sound with Unsteady Transonic Flow in a Nozzle," AIAA Paper 98-2213, June 1998.

[10]Casalino, D., "An Advanced Time Approach for Acoustic Analogy Predictions," *Journal of Sound and Vibration* (to be published).

[11]Williamson, C. H. K., "Oblique and Parallel Modes of Vortex Shedding in the Wake of a Circular Cylinder at Low Reynolds Numbers," *Journal of Fluid Mechanics*, Vol. 206, 1989, pp. 579–627.

[12]Szepessy, S., and Bearman, P. W., "Aspect Ratio and End Plate Effects on Vortex Shedding from a Circular Cylinder," *Journal of Fluid Mechanics*, Vol. 234, 1992, pp. 191–217.

[13]Casalino, D., "Analytical and Numerical Methods in Vortex-Body Aeroacoustics," Ph.D. Dissertation, Dipartimento di Ingegneria Aeronautica e Spaziale, Politecnico di Torino, Turin, Italy, and Laboratoire de Mécanique des Fluides et d'Acoustique, Ecole Centrale de Lyon, Ecully Cedex, France, May 2002.

[14]Kato, C., and Ikegawa, M., "Large Eddy Simulation of Unsteady Turbulent Wake of a Circular Cylinder Using the Finite Element Method," *Advances in Numerical Simulation of Turbulent Flows*, Fluids Engineering Div., Vol. 117, American Society of Mechanical Engineers, Fairfield, NJ, 1991, pp. 49–56.

[15]Roshko, A., "Perspectives on Bluff Body Aerodynamics," *Journal of Wind Engineering and Industrial Aerodynamics*, Vol. 49, No. 1–3, 1993, pp. 79–100.

[16]Amiet, R. K., "Refraction of Sound by a Shear Layer," *Journal of Sound and Vibration*, Vol. 58, No. 3, 1978, pp. 467–482.

W. J. Devenport
Associate Editor